



Contents lists available at ScienceDirect

Journal of the Mechanics and Physics of Solids

journal homepage: www.elsevier.com/locate/jmps

Poisson's ratio and residual strain of freestanding ultra-thin films



Gayatri K. Cuddalorepatta^{a,*}, Wim M. van Rees^{a,b}, Li Han^c, Daniel Pantuso^c,
L. Mahadevan^a, Joost J. Vlassak^a

^aSchool of Engineering and Applied Sciences, Harvard University, Cambridge, MA 02138, USA

^bDepartment of Mechanical Engineering, Massachusetts Institute of Technology, Cambridge, MA 02139, USA

^cTechnology Manufacturing Group, Intel Corporation, Portland, OR USA

ARTICLE INFO

Article history:

Received 24 July 2019

Revised 28 November 2019

Accepted 7 December 2019

Available online 16 December 2019

Keywords:

Ultra thin film
Freestanding
Poisson's ratio
Residual strain
Residual stress
Transverse wrinkling
Stretched bridges
XeF₂ etch
Copper

ABSTRACT

The Poisson's ratio and residual strain of ultra-thin films (<100 nm) are characterized using the phenomenon of transverse wrinkling in stretched bridges. The test methodology utilizes residual stress driven structures and easy to replicate clean-room fabrication and metrology techniques that can be seamlessly incorporated into a thin-film production assembly line. Freestanding rectangular ultra-thin film bridges are fabricated using dimensions that generate repeatable transverse wrinkling patterns. Numerical modeling based on the non-linear Koiter plate and shell energy formulation is conducted to correlate the Poisson's ratio and residual strain to the measured wrinkling deformation. Poisson's ratio affects the peak amplitudes without significantly changing the wavelength of the wrinkles. By contrast, the strain affects both the wavelength and amplitude. The proof of concept is demonstrated using 65 nm thick copper films. A Poisson's ratio of 0.34 ± 0.05 and a tensile residual strain of $(6.8 \pm 0.8) \times 10^{-3}$ are measured. The measured residual strain is in good agreement with the residual strain of $(7.1 \pm 0.2) \times 10^{-3}$ measured using alternate residual stress-driven test structures of the same films.

© 2019 Elsevier Ltd. All rights reserved.

1. Introduction

Current technology in microelectronics utilizes thin films that are a few tens of nanometers in thickness. The reliability of microelectronics devices depends on the mechanical behavior of these ultra-thin films. The mechanical properties of a material are determined by the interaction of the microstructural length scale and the characteristic length scale of the dominant deformation mechanism (Arzt, 1998; Barai and Weng, 2009; Hahn and Meyers, 2015). These length scale parameters and their coupling are further affected when the thickness of the film approaches the scale of these parameters. In addition, thin films that exhibit scale-dependent mechanical behavior (Arzt, 1998; Haque and Saif, 2002; Huang and Spaepen, 2000; Liang et al., 2002; Xiang and Vlassak, 2006), have been observed to deviate from existing trends (Arzt, 1998; Hahn and Meyers, 2015; Haque and Saif, 2002). Thus, the properties of nanoscale materials need to be characterized as a function of the thickness of the film and fabrication protocols.

* Corresponding author.

E-mail address: gayatric@seas.harvard.edu (G.K. Cuddalorepatta).

The current study focuses on the measurement of Poisson's ratio and residual strain in freestanding ultra-thin films (<100 nm thick). The methodology applies to films with a tensile residual stress. The test design we propose is motivated by the requirement of an in-line metrology tool that (i) can be seamlessly implemented in a thin-film production line immediately after fabrication, without any additional sample preparation, (ii) uses easy-to-replicate clean-room based fabrication and metrology tools, that are readily available in a semi-conductor production line, (iii) does not require external sample loading setups or dedicated/sophisticated test setups for sample characterization and (iv) is applicable for testing of a wide range of materials. To this end, we propose to use residual-stress-driven test structures of freestanding ultra-thin films, thereby eliminating sample loading mechanisms and fixtures (Senturia et al., 1987; Vayrette et al., 2014). The deformation of the released freestanding structures is readily captured using an optical profiler without additional sample preparation.

Typically the residual strain in films can be measured using methods such as the wafer curvature technique (Freund et al., 1999; Stoney, 1909), X-ray diffraction and Raman spectroscopy methods (Ager and Drory, 1993) (see Refs. (Gunda et al., 2017; Huang et al., 2013) for a review of residual stress characterization techniques). In addition to these established techniques, the phenomenon of buckling instability is exploited using thin films on compliant substrates (Chen and Hutchinson, 2004; Mei et al., 2007; Stafford et al., 2004), to measure the residual strain in ultra-thin films with a high precision (Chung et al., 2009). Poisson's ratio in thin films has been characterized using techniques such as bulge testing (Vlassak and Nix, 1992) and X-ray diffraction (Chang et al., 2009; Fu et al., 2013; Le Rouzic et al., 2012). Though these techniques have merits, they are challenging to implement seamlessly as in-line thin-film characterization techniques in a semiconductor production environment.

In order to measure Poisson's ratio and residual strain simultaneously using residual stress-driven structures, we exploit the phenomenon of transverse wrinkling in stretched bridges that is observed in large area membranes such as sunshields, radars, inflatable antennas and solar sails in space craft applications (Sakamoto and Park, 2005; Talley et al., 2002; Wong and Pellegrino, 2006a; Zheng, 2009). When rectangular sheets are clamped at the short ends and stretched along the longitudinal axis, wrinkling occurs in the transverse direction at the mid section of the sheets. This wrinkling is a consequence of compressive stresses established in the transverse direction to balance the restriction of the Poisson contraction at the end constraints (Healey et al., 2013; Nayyar et al., 2011; 2014; Wong and Pellegrino, 2006b; Zheng, 2009). Studies on wrinkling of such stretched bridges show that the wrinkling amplitude and wavelength can be related to Poisson's ratio ν , tensile strain, and sample geometry (Cerda and Mahadevan, 2003; Puntel et al., 2011; Wong and Pellegrino, 2006a). To this end, we propose to solve the inverse problem of determining Poisson's ratio and stretch/residual strain, by measuring the transverse wrinkling induced in ultra-thin film bridges when the tensile residual stress in the film is released.

While this phenomenon has been widely studied for macro-scale materials (thicknesses > 100 μm (Cerda and Mahadevan, 2003; Nayyar et al., 2014)), wrinkling in materials with thickness in the range of 100 nm or less have not been explored thus far. Here we demonstrate the technique in 65 nm thick copper films, using a combination of experiments and simulations. We use the work by Nayyar et al. (2011) for insights on the in-plane aspect ratios required for the onset of wrinkling in freestanding single-layer ultra-thin film bridges. When the ultra-thin films are released from the underlying silicon substrate and made freestanding, the tensile residual stress in the films is relieved and induces wrinkling patterns in the transverse direction with repeatable and measurable wavelength, amplitude, and wave numbers.

Numerical simulations based on the non-linear Koiter elastic thin plate and shell energy formulation are conducted by replicating the geometry and constraints in the fabricated freestanding test bridge. A parametric study of Poisson's ratio and the residual strain is conducted, and their influence on the wrinkling parameters is provided. The wrinkling parameters from the experiments are correlated to the modeling predictions to determine the Poisson's ratio and tensile residual strain in the ultra-thin film.

The layout of the paper is as follows. Section 2 describes the test structures, experiment, and, the numerical modeling. The experimental and numerical modeling results are discussed in Section 3. The Poisson's ratio and residual strain measured in the ultra-thin test film using the proposed technique are reported. Section 4 discusses the scope of the proposed technique and the conclusions of the study are provided in Section 5.

2. Materials and methods

The proof of concept of the proposed test methodology is provided using sputter deposited copper thin films with a thickness of 65 nm. The details of the test structure geometry, fabrication and metrology tools, numerical modeling approach, and recommendations for successful fabrication of freestanding films are provided in this section. A detailed numerical simulation is conducted using the geometry of the fabricated test structures and the effect of the complaint support conditions of the fabricated freestanding test bridges is studied. Using the numerical model, the influence of Poisson's ratio and residual strain on the experimentally measured wrinkling parameters is studied and compared with existing studies in the literature.

2.1. Geometry of test structure and test material

Systematic studies were conducted by Nayyar et al. (2011), Nayyar (2013) and Zheng (2009) to understand the conditions for the onset of wrinkling in clamped, stretched polyethylene bridges. They found that transverse wrinkling occurs in rectangular bridges only for select combinations of in-plane aspect ratio (length to width), thickness, and strain. When the

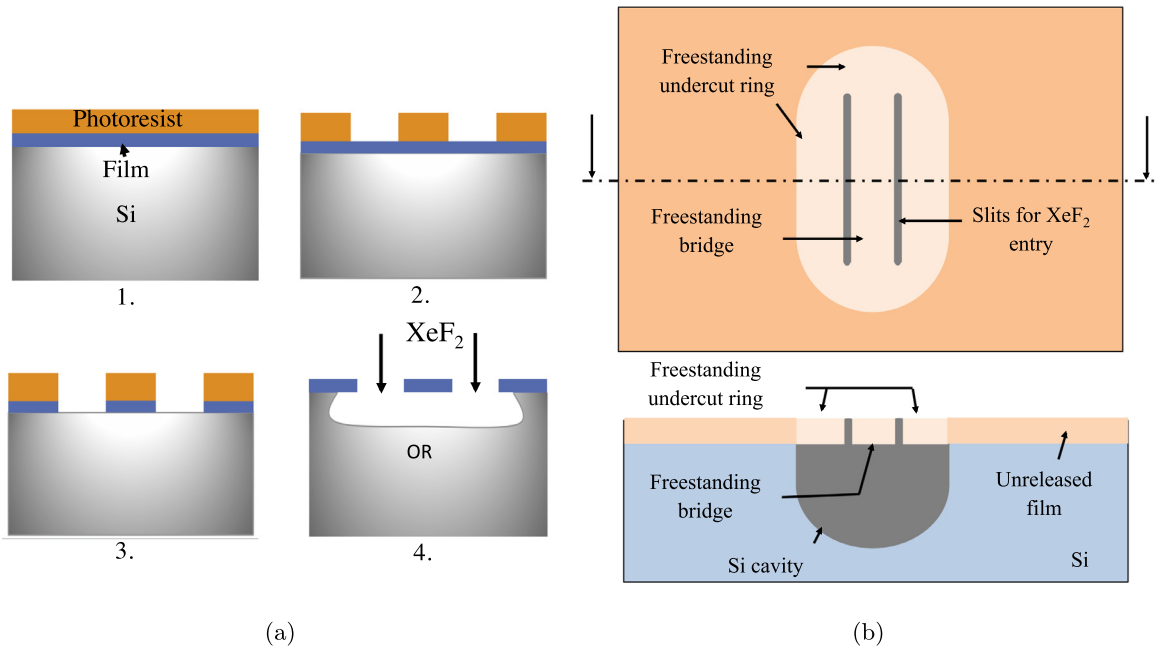


Fig. 1. (a) Schematic of fabrication process flow for freestanding single layer bridges. Refer to the text for description on Steps 1–4. (b) Schematic of the top and cross-sectional view of a freestanding test bridge. A freestanding undercut ring that is approximately the width of the bridge surrounds the bridge due to the isotropic nature of Si etch (Step 4 in Figure (a)).

in-plane aspect ratio is larger than one, transverse compressive stresses are established to balance the restriction of Poisson's contraction at the clamped ends (Nayyar, 2013; Nayyar et al., 2011). Based on their study, an in-plane aspect ratio of two was seen to produce transverse compressive stresses and wrinkling patterns, that were measurable in magnitude and spread (for strains as low as 1%). The thickness of the bridges in their study is larger than $100\ \mu\text{m}$, which is significantly thicker than that in the current study.

In our experiments, freestanding test structures of 65 nm copper with a width less than $35\ \mu\text{m}$ and in-plane aspect ratios as high as two, do not exhibit significant wrinkling except for a slight bulging of the film in the mid-section and curling at the free edges in the transverse direction. Furthermore, to characterize the wrinkling patterns effectively, it is desirable to have a width that can accommodate more than a single wave. Hence test bridges with a width of $150\ \mu\text{m}$ and an aspect ratio slightly larger than four (length of $650\ \mu\text{m}$) were fabricated to yield a wrinkling pattern with seven distinct measurable peaks.

2.2. Fabrication

The process steps for the fabrication of copper test bridges are described here. Fig. 1a illustrates the process flow. Detailed process information is provided in Appendix A. The fabrication process flow for the single-layer freestanding bridges starts with a (100) silicon wafer. The wafer is cleaned using a buffered oxide etch to remove the native oxide, followed by argon plasma cleaning. A copper film with a nominal thickness of 63 nm is deposited onto the substrate using a magnetron sputter deposition system (AJA International Inc.) with a base pressure of 2×10^{-7} Torr and an Ar working pressure of 3 mTorr. A layer of titanium of approximately 2 nm is deposited immediately prior and after the copper deposition. Titanium serves as an adhesion layer and a diffusion barrier layer. The top titanium layer is etched in the final stages of fabrication, resulting in a test film stack with a total thickness of 65 nm. A positive photoresist (Shipley 1818) is then spin coated on top of the deposited film (step 1), followed by a soft bake at $115\ ^\circ\text{C}$. The photoresist is patterned and exposed using a maskless aligner (Heidelberg μpG MW-3). After exposure, the substrates are baked at $115\ ^\circ\text{C}$, developed in CD50 developer (<1 min), rinsed in deionized (DI) water, and dried with nitrogen (step 2).

After patterning, the titanium is etched using a CF_4 - based reactive ion etching (Southbay RIE). The copper film is subsequently etched using a wet etchant (80 wt% phosphoric acid, 5 wt. % nitric acid, 5 wt. % acetic acid and 10 wt. % distilled water), as shown in step 3. The etched structures are rinsed in DI water and the photoresist is stripped using acetone followed by isopropyl alcohol in an ultrasound bath. The substrates are baked at $100\ ^\circ\text{C}$ for 2 minutes to eliminate residual moisture and the titanium adhesion layer is etched using reactive ion etching. In a final step (step 4), the substrates undergo a dehydration bake and the bridges are released from the substrate using an isotropic XeF_2 etching system (Xactix X-SYS EXP Xetch). The resulting bridges are a bi-layer stack of 63 nm thick Cu film on top of a 2 nm thick titanium layer with a total thickness of 65 nm. The Si etch process that releases the ultra-thin film to the freestanding state is the crucial step in

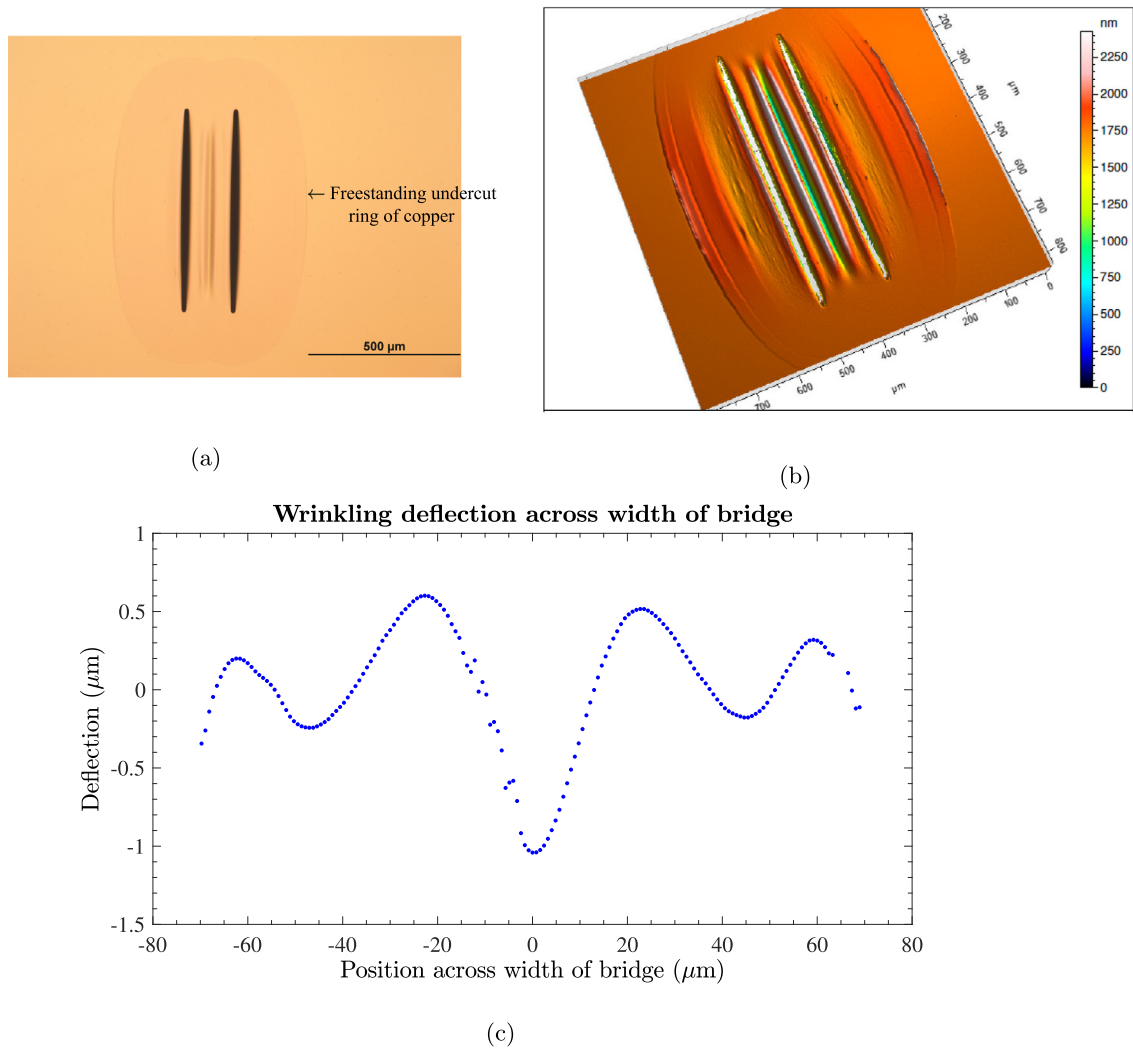


Fig. 2. (a) Optical image of the test sample showing a freestanding bridge of 65 nm of copper. The bridge is supported by a compliant freestanding undercut ring of copper. (b) Corresponding deflection contour map, as measured by the white light interferometry based optical profiler. Transverse wrinkling with distinct peaks and valleys is observed across the bridge. (c) The wrinkling profile extracted across the width of the bridge from the contour map in (b). The amplitude is seen to decay across the width of the bridge.

the sample fabrication process. Bridges with in-plane dimensions on the order of hundreds of micrometers and a thickness of 65 nm are obviously quite fragile to fabricate and do not easily survive in freestanding state. Guidelines are provided in [Appendix A](#), for the Si etch process in order to fabricate robust and defect-free, freestanding ultra-thin film bridges.

2.3. Freestanding test structures and metrology

Due to the isotropic nature of the Si etch process, the Si support is undercut and the freestanding bridge is supported by a compliant freestanding ring of copper. [Fig. 1b](#) illustrates the cross-sectional view of the freestanding undercut film surrounding the freestanding bridge. This ring is referred to as the undercut ring in this study. [Fig. 2a](#) shows an optical image of a freestanding bridge of passivated copper with a total thickness of 65 nm, a length of 650 μm and width of 150 μm. The supporting undercut ring extends to approximately 150 μm around the bridge. The support conditions in the bridges are far from the ideal clamped supports that are assumed in the analytical models available for transverse wrinkling of stretched freestanding bridges ([Cerdea and Mahadevan, 2003](#); [Puntel et al., 2011](#)). Hence, in the current study, we model the full geometry of the freestanding ultra-thin film bridges with the supporting undercut film in the numerical model ([Section 2.4](#)).

The wrinkling deflections across the freestanding bridges are measured without any additional sample preparation using a non-contact optical profiler based on white light interferometry (Taylor Hobson CCI HD). A total of six bridges were characterized and two measurements are made across the same sample. The wrinkling deformation was also characterized using

AFM (Veeco AFM) to verify the accuracy of the optical profiler. Peak amplitudes and wavelengths were within 5% between both measurement techniques. Fig. 2b and c show the measured contour graph and the surface profile of the out-of-plane deflections of the freestanding bridges measured by the optical profiler. The surface profile is extracted from the mid-section of the bridge.

The freestanding bridges show a crisp and repeatable wrinkling pattern in the transverse direction with seven distinct peaks and valleys. The amplitude of the wrinkles decays from the center to the edge of the bridge (similar to the study by Puntel et al. (2011)), and the wrinkling profile is symmetric across the width. Wrinkling profiles extracted from the 3-D contour data of the bridges are found to be invariant across locations spanning $\pm 20\mu\text{m}$ from the longitudinal mid-section of the bridge. For measuring the wavelength, we use the eigenspace analysis method available in the theory of signal processing and determine the frequency content of a signal (Oppenheim and Schaffer, 2009). We implement this technique using the in-built eigenspace analysis function available in the signal processing toolbox in MATLAB Signal Processing Toolbox. The peak amplitude is determined as the maximum deflection in the wrinkling profile (zero being the undeformed flat substrate).

2.4. Modeling

The wrinkling behavior is characterized using the wavelength and amplitude of the deflection. These parameters have been described using closed-form relationships in terms of the applied stretch, Poisson's ratio and geometric dimensions by Cerda and Mahadevan (2003) and Puntel et al. (2011) as

$$\lambda = \frac{\sqrt{2\pi Lt}}{[3\varepsilon(1-\nu^2)]^{\frac{1}{4}}} \quad (1)$$

$$A_{peak} = \sqrt{\nu Lt} \cdot \left[\frac{16\varepsilon}{3\pi^2(1-\nu^2)} \right]^{\frac{1}{4}}, \quad (2)$$

where λ is the wavelength, A is the amplitude, ν is Poisson's ratio, ε is the tensile strain, L is the length of the bridge, and t is the thickness of the test bridge. These analytical relationships are compared with a numerical model developed in this study, based on the principle of energy minimization. The numerical model studies the transverse wrinkling that occurs in the bridge structures by modeling the compliant support conditions created by the undercut ring in the experimental test structures. Complete details of the model will be available in future publications and only the relevant details are included here.

The non-linear elastic energy of continuous, isotropic thin plates, can be formulated in terms of stretching and bending of the plate mid-surface. Here we use the Koiter shell model, which can be derived based on three assumptions. The first assumption is that the normals to the mid-surface of the plate are inextensible and remain normal, also known as the Kirchhoff-Love assumption. The second and third assumptions are that the thickness of the plate is much smaller than the other two dimensions and the stretching strains are much smaller than unity. The energy can be then derived in a curvilinear coordinate system to handle large deformations and complex geometries (Simo and Fox, 1989). Lower-order approximations, such as the well-known Föppl-Von Karman model, can be derived from this energy (Audoly and Pomeau, 2010; van Rees et al., 2017).

We use a discrete form of the Koiter energy, based on a triangulated representation of the plate mid-surface to represent the geometry (Weischedel et al., 2012). For each triangle, we compute the local stretching and bending energy associated with any deformation of its specified, strain-free rest configuration. Summing up the energy over all triangles provides the total elastic energy of a global deformation, which converges to the value of a continuous plate as the number of triangles increases. Given a rest configuration, material properties, and boundary conditions, a quasi-Newton minimization method (Liu and Nocedal, 1989) yields the configuration of the plate that minimizes the elastic energy. The discretization follows the work of Weischedel et al. (2012) for the shear-free, discrete Kirchhoff case. As discussed there, the approach is closely related to a geometric reformulation of the constant strain triangle (CST) for the membrane energy, and a the Morley element (Morley, 1971) for the bending energy.

To tackle the problem considered here, we first model the geometry of the bridge (see Fig. 3, left). We start out with the undercut ring, modeled as a rectangular sheet with a length of $650\mu\text{m}$ and a width of $150\mu\text{m}$, capped with elliptical arcs on its short sides. The bridge is modeled by creating two parallel slits in the sheet, creating a rectangular segment inside the ring whose long edges are free, and short edges are connected to the outer film. The dimensions of the elliptical undercut geometry are chosen to approximate the test structure as well as possible. This model is discretized using a triangle mesh (Shewchuk, 1996), as shown in Fig. 3 (right). A constant isotropic residual strain is applied by modifying the rest configuration of each triangle to be a rescaled version of its realization in the initial condition described above, similar to the procedures used to model non-Euclidean plates (Efrati et al., 2009) as implemented in our solver (Chen et al., 2018; van Rees et al., 2018; 2017). Furthermore, we impose clamped boundary conditions at the outer circumference of the suspended ring. Given this geometry, and rest configuration, we run the minimization algorithm to find the minimum-energy, equilibrium configuration of the strained sheet. Appendix B gives further details of the formulations described here.

For all simulations, the film thickness is set to a value of 65nm , as in the experiments. Poisson's ratio is varied between 0.24 – 0.36 , and the residual strain is varied from 0.1% to 2% . The effect of Poisson's ratio at a strain of 0.5% is explored for Poisson's ratio ranging from 0.15 to 0.45 . Young's modulus is irrelevant for this problem, since there are no external

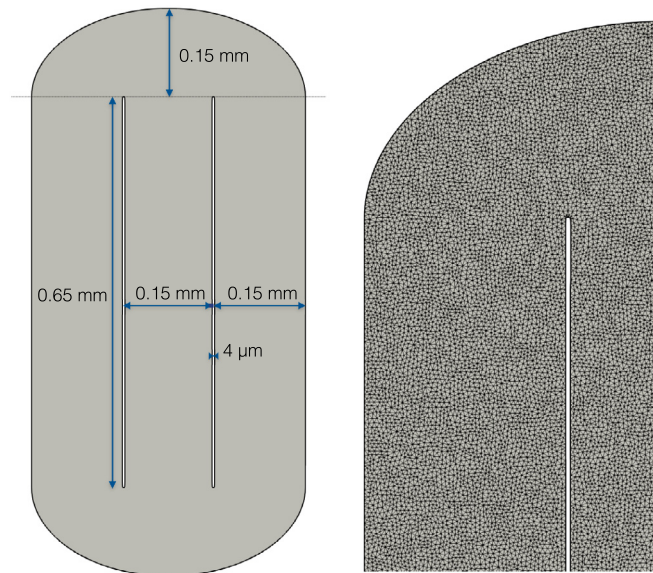


Fig. 3. The geometry of the bridge as modeled for simulations. The right picture shows a close-up of the triangulation of the top-left corner of the geometry, using 80000 triangles. The results presented in the study use a finer mesh of around 320000 triangles.

forces applied to the sheet. Since there is no inherent notion of top and bottom in this setup, we flip the wrinkling profile whenever necessary to compare with the experiments.

We first conducted a mesh refinement study, to evaluate the sensitivity of the results to changing number of triangles in the mid-surface discretization. The lowest resolution has approximately 80,000 triangles, and we increase this number by a factor of two until we reach 640,000 triangles. At the coarsest mesh density of around 80,000 elements, the wrinkle pattern is significantly different from the measured wrinkling profile. The deformation is anti-symmetric about the center of the bridge with amplitudes that are half the magnitude of those in the experiment. Increasing the mesh density by a factor of four results in a symmetric wrinkling profile that matches the shape and magnitude of the measured wrinkles.

The sensitivity of the numerical model to mesh density is illustrated in Fig. 4a. For each resolution, we compute the wrinkling profile across the bridge corresponding to a Poisson's ratio of 0.3 and a residual strain of 0.5%. The mesh resolutions in the figure correspond to 80,000 elements for the coarsest mesh (1x) to 640,000 elements for the finest mesh (4x). In addition to the mesh resolutions presented in Fig. 4a, we also simulated the model using about sixteen times the coarsest mesh density (not shown here) with around 1.2×10^6 elements. The change in peak amplitude from the second-highest resolution with approximately 320,000 elements to the highest resolution is well within the experimental measurement error. Hence for this study, the second finest mesh density (termed as Mesh resolution-3x in the Fig. 4a) is used to determine the wrinkling parameters of the bridge. At this resolution, the average sidelength of each triangle is approximately 1.5 μm . Fig. 4b shows a contour plot of the wrinkling deformation of the bridge using these mesh resolution parameters, which is similar to that observed experimentally (see Fig. 2b). We further notice an asymmetry in the wrinkling profiles of Fig. 4a. This asymmetry is consistent with the work by Healey et al. (2013), who perform a parametric global bifurcation analysis on the wrinkling of stretched rectangular sheets. They found that, for a given strain, there exists a family of energetically equivalent, stable solutions with a continuous range of possible phase angles. These include symmetric and antisymmetric wrinkling patterns, as well as any phase in between these extremes. These different equivalent solutions appear to be characterized by the same maximum wrinkling amplitude and wrinkling wavelength. This is consistent with our numerical results, where we find minimum energy conditions that are not biased towards any particular symmetry condition, yet are characterized by consistent peak amplitudes and wrinkling wavelengths.

3. Results and discussion

The accuracy of the numerical model in capturing the measured wrinkling deformation is discussed in this section. The Poisson's ratio and residual strain measured in 65 nm thick copper films using the proposed technique are presented.

3.1. Wrinkling deflection: experiment versus numerical model

The wrinkling profiles obtained from the test bridges are compared with those obtained from the numerical model in Fig. 5. It is seen that Poisson's ratio has a large influence on the amplitude, but not on the wave length. For example at a

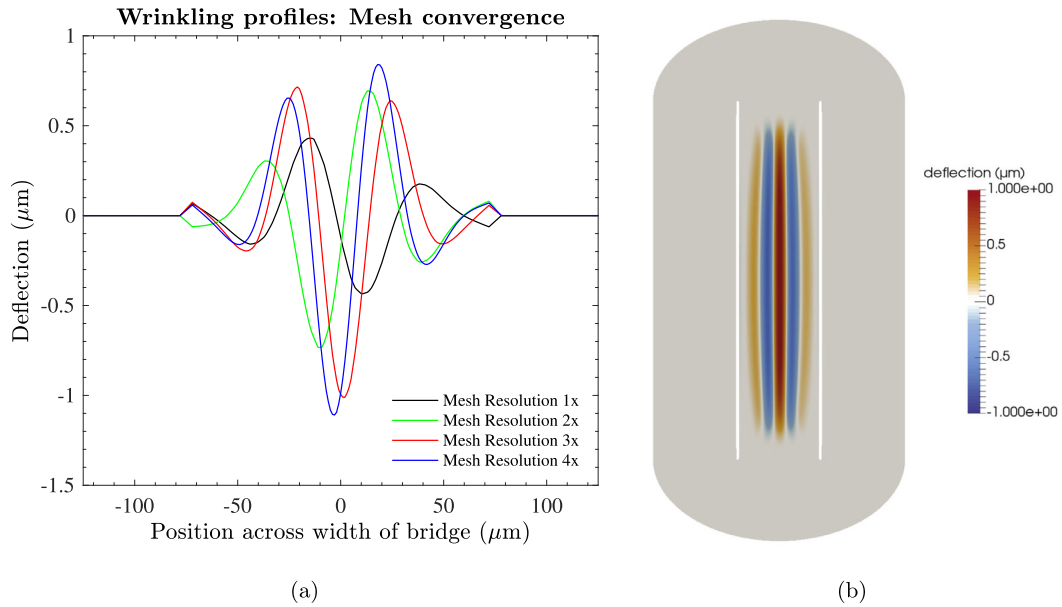


Fig. 4. (a) Mesh convergence study showing the wrinkling profiles across the bridge, using a Poisson's ratio of 0.3 and a residual strain of 0.5%. The legends Mesh Resolution 1x, 2x, 3x and 4x correspond to 80,000, 160,000, 320,000 and 640,000 elements. (b) Contour map of the out-of-plane deformation for the bridge derived from the numerical model using the second finest mesh density denoted by Mesh Resolution 3x in Figure (a). The wrinkling profile presented corresponds to a Poisson's ratio of 0.3 and a tensile residual strain of 0.5%.

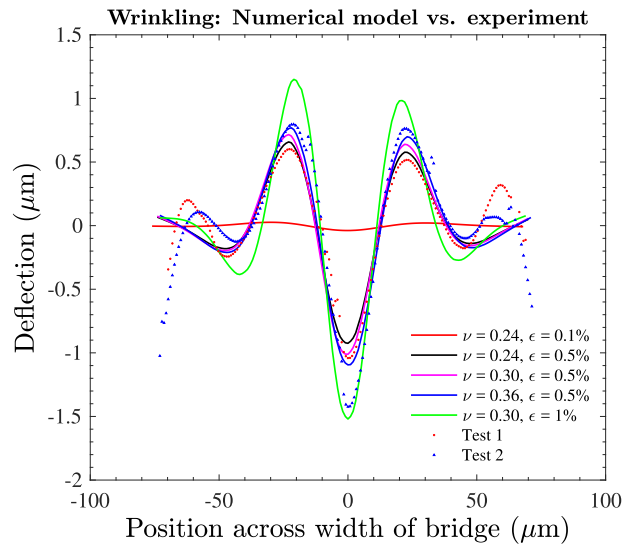


Fig. 5. Wrinkling profiles predicted by the numerical model as a function of Poisson's ratio and residual strain. The mesh density corresponds to around 320,000 elements (denoted by Mesh Density 3x in Fig. 4a). Two representative test measurements as measured by the optical profiler are included. These data qualitatively show the upper and lower bounds of the wrinkling deflections measured across six test samples. The numerical model follows the measured wrinkling deflections well except at the free edges, for $\nu=0.3$ and stretch =0.5%.

constant strain of 0.5%, a change of 17% in ν results in 8% change in the peak amplitude, while the wavelength changes by 0.1%. By contrast, both the wavelength and amplitude are sensitive to the residual strain.

It is evident from Fig. 5 that the wrinkling patterns simulated by the numerical model are in qualitative agreement with the measured wrinkling profile, although the amplitudes of the smaller peaks follow the experimental wrinkles less closely compared to the central peak. While the peak amplitudes and wavelength match closely, the experimental samples show additional wrinkles at the free edges of the bridge, that are not captured by the numerical model. The deviations near the free edges are likely caused by a stress gradient through the thickness of the film. The edges of the bridge width ($\pm 5 \mu\text{m}$) are hence eliminated for evaluating the wavelength of wrinkling.

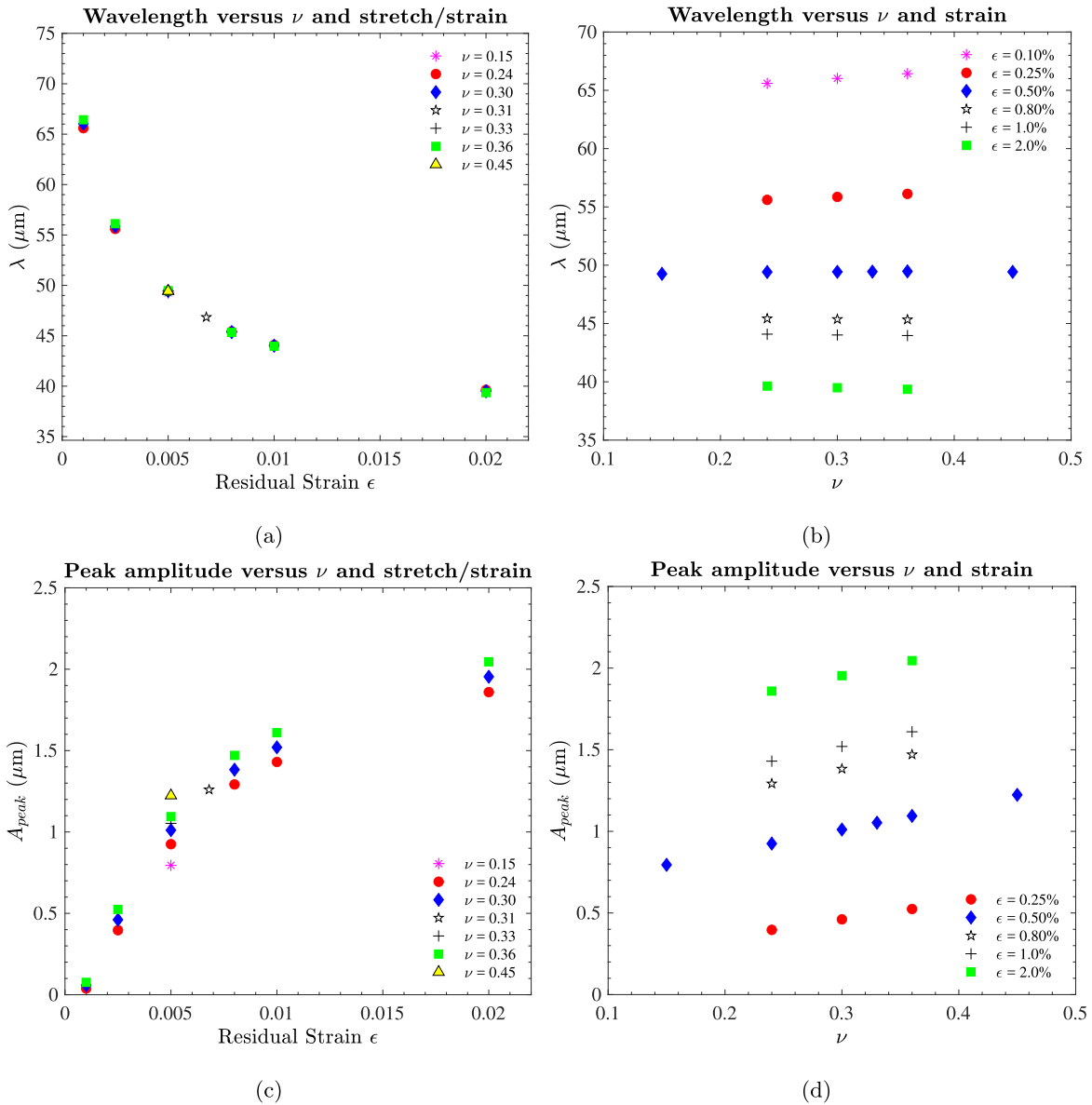


Fig. 6. (a) Wavelength of wrinkling as a function of ν and stretch/tensile residual strain. (b) The wavelength is invariant with ν . (c) Peak amplitude of wrinkling as a function of ν and stretch/tensile residual strain. The peak amplitude scales with ν , as shown in (d).

3.2. Wavelength and peak amplitude: variation with Poisson's ratio and residual strain

The wavelength measured from the test bridges is $47.02 \pm 2.62 \mu\text{m}$ and the peak amplitude is $1.30 \pm 0.21 \mu\text{m}$. The errors reported here correspond to the standard deviation in the measurements across six samples. The variation of the wavelength and peak amplitude as a function of Poisson's ratio and strain in the numerical model are presented in Fig. 6a–d respectively. It is clear from Fig. 6a and b that the wavelength decreases with increasing strain, but is relatively unchanged with Poisson's ratio. The observed dependencies of wavelength agree with the studies by Nayyar et al. (2011, 2014). The peak amplitude depends on both residual strain and Poisson's ratio, with the effect of Poisson's ratio increasing at strain values greater than 0.1%. The peak amplitude is seen to scale linearly with Poisson's ratio, over the range of Poisson's ratios modeled in this study (Fig. 6d).

3.3. Poisson's ratio and residual strain of 65 nm copper films

The measured wrinkling profile is in qualitative agreement with the profile simulated by the numerical model when Poisson's ratio and residual strain are in the range of 0.3 and 0.5% respectively (Fig. 5). To evaluate the Poisson's ratio

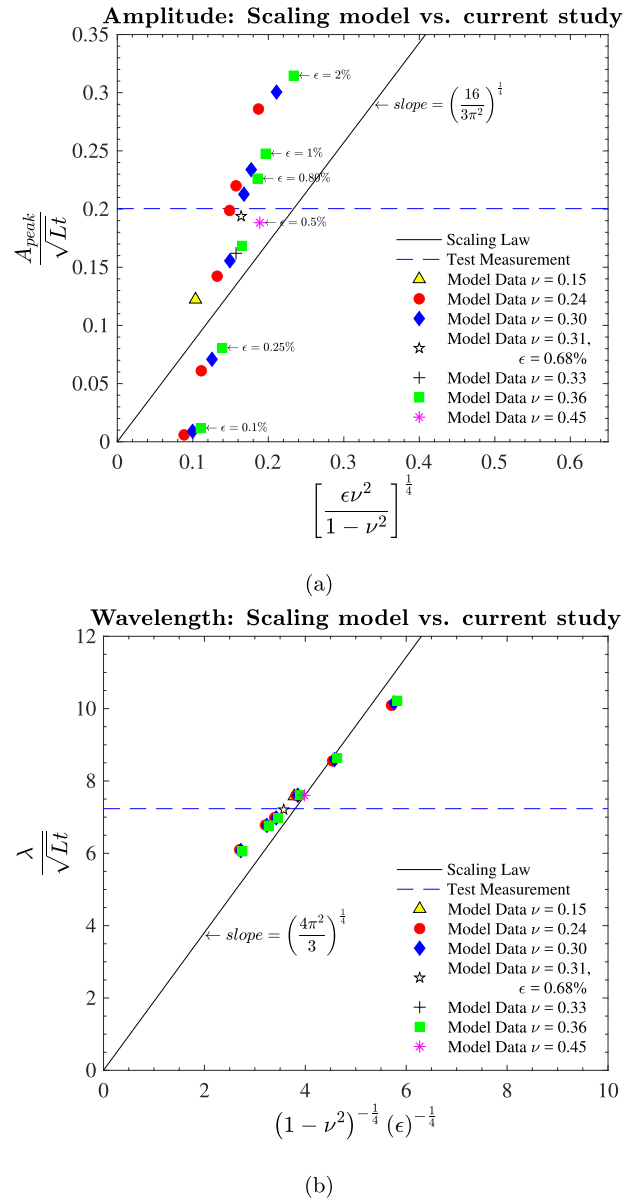


Fig. 7. Comparison of the normalized peak amplitude and wavelength from current numerical model versus the strain and Poisson's descriptions by the scaling law from Ref. (Cerde and Mahadevan, 2003). (a) The normalized peak amplitude predicted from the numerical model deviates significantly from the ν and residual strain dependence described by the scaling law at strains larger than 0.1%. (b) The numerical model's wavelength shows a small deviation in slope from the scaling's law dependence on ν and stretch or tensile residual strain. The mean values of the peak amplitude and wavelength measured from 65 nm thick copper samples is shown by the dashed line in (a) and (b).

and residual strain of the test film corresponding to the measured wavelength and amplitude more precisely, we explore available studies in literature that describe the influence of Poisson's ratio (ν) and stretch/tensile strain (ϵ) on the wrinkling parameters (Cerde and Mahadevan, 2003; Healey et al., 2013; Nayyar et al., 2011; 2014; Zheng, 2009).

We first evaluate if the scaling laws developed for rectangular sheets with clamped support (Cerde and Mahadevan, 2003), can adequately describe the wrinkling of the bridges with compliant support conditions seen in our study. Fig. 7 shows the normalized amplitude and wavelength as a function of non-dimensional functions of the residual strain and Poisson's ratio (Eqs. (1)-(2)). If the scaling relationships are valid, then the normalized amplitude and wavelength should collapse into a single curve. As illustrated in Fig. 7a, the normalized peak amplitude deviates significantly from the scaling relationship's dependence on strain and ν . The normalized wavelength also deviates from the expected slope of $\left(\frac{4\pi^2}{3}\right)^{\frac{1}{4}}$ (Fig. 7b). The scaling law for the wavelength has a very small dependence on ν , given by $(1 - \nu^2)^{-\frac{1}{4}}$. The numerical results for the bridges modeled in our study, show that the wavelength does not depend on ν within the error of the numerical

model (Fig. 6a-b). The experimentally measured peak amplitude and wavelength do not yield reasonable values of Poisson's ratio using the scaling laws. However, the residual strain from the scaling relations is comparable to that obtained from the numerical results.

We hypothesize that the discrepancy between our numerical results and the scaling laws are primarily due to the support boundary conditions and the finite aspect ratio of our bridges. The analytical model (Cerda and Mahadevan, 2003) assumes clamped boundary conditions and does not consider edge effects due to finite-width sheets, which is in conflict with our experimental and numerical configuration. Further, our numerical simulations provide an indication that there exists a critical threshold for the strain, below which no wrinkling occurs. This is consistent with the results of Healey et al. (2013), but is not considered in the analytical scaling laws (Cerda and Mahadevan, 2003). Such a critical strain threshold would explain the discrepancy at low strain values. Lastly, our experimental and numerical configuration is characterized by an isotropic residual strain, whereas the scaling analysis (Cerda and Mahadevan, 2003) considers transverse wrinkling due to uniaxial tension. The transverse compressive displacement would then change to being proportional to $(1 + \nu)\epsilon$, rather than $\nu\epsilon$ as assumed in (Cerda and Mahadevan, 2003), which would slightly change the scaling laws for the peak amplitude A_{peak} .

The numerical model results show that the normalized wavelength depends only on strain to a good approximation and is described fairly well with a power law dependence on strain as in the scaling laws. We obtain additional insights from the dependence of amplitude on ν , ϵ , and geometry from the systematic studies conducted (Nayyar et al., 2011; 2014), (Healey et al., 2013), and (Zheng, 2009). Their studies show that the amplitude does not vary monotonically with applied strain, but instead reaches a maximum before decreasing (similar to the response of the test case we studied in Appendix C). The strains explored in the above studies are fairly large and on the order of 10% or higher (Nayyar et al., 2011; 2014; Zheng, 2009), which are relevant for elastomer materials. In our study, however, we focus on elastic strains that are typical of residual strains in thin films used in semiconductor applications. For our test bridge geometry and support conditions, we have modeled strains as high as 2% (which are larger than the permissible elastic strains in thin films) and find that the response in this strain range corresponds to the initial region where the amplitude increases with strain.

To investigate if the non-monotonic behavior of amplitude with strain is captured in our numerical model, we modeled a test case as in Healey's study (Healey et al., 2013) and explore the behavior at strains upto 15%. We verify that similar trends as those observed by Healey et al. (2013) are obtained using our numerical model; the amplitude increases initially with strain and subsequently drops after reaching a maximum (see Appendix C). Nayyar et al. also show that the onset of wrinkling occurs for select aspect ratios and that the amplitude is dependent on the length to width and the width to thickness aspect ratios. They find that the amplitude follows a non-monotonic dependence on the length to width aspect ratio and that the amplitude increases with the width to thickness aspect ratio, within the cases that they studied (Nayyar et al., 2014).

Using the above insights, we describe the wrinkling parameters as a function of ϵ and ν for the geometric configuration used here as:

$$\frac{\lambda}{\sqrt{Lt}} = k_1 \epsilon^{n_0} \quad (3)$$

The constants $k_1 = 3.02 \pm 0.03$, and $n_0 = -0.18 \pm 1.7 \times 10^{-3}$. The wavelength follows a power law dependence on strain with a mean exponent of -0.18 compared to an exponent of -0.25 from the scaling law. Since the wavelength depends on the strain only, the residual strain can be uniquely determined from the wavelength relation alone.

The peak amplitude, A_{peak} is given by

$$\frac{A_{peak}}{w} = \frac{p_1(\nu)\epsilon + p_2(\nu)}{\epsilon + p_3(\nu)} \quad (4)$$

where each $p_i(\nu) = a_i\nu + b_i$. The constants $a_1 = 7.07 \times 10^{-3} \pm 5.2 \times 10^{-6}$, $b_1 = 1.57 \times 10^{-2} \pm 1.45 \times 10^{-6}$, $a_2 = (8.27 \pm 8.40) \times 10^{-6}$, $b_2 = (-1.86 \pm 0.26) \times 10^{-5}$, $a_3 = (-8.61 \pm 1.86) \times 10^{-3}$, and $b_3 = (8.57 \pm 0.57) \times 10^{-3}$. The values of these constants depend on the aspect ratios of the bridges and are only valid for the geometry and aspect ratios of the bridges used in our study. In Eqs. (3)-(4), the length (L), width (w) and thickness (t) of the bridges are 650 μm , 150 μm and 65 nm respectively.

Using the above expressions with the average values and the error of the distribution of the means of each wrinkling parameter (peak amplitude and wavelength respectively), we find a Poisson's ratio of 0.34 ± 0.05 and a tensile residual strain of $(6.8 \pm 0.8) \times 10^{-3}$ in the 65 nm copper film. These values are also presented in Fig. 8a and b. Poisson's ratio measured in this study compares well with a value of 0.37 ± 0.05 measured for 2.5 μm thick polycrystalline copper films (Huang, 1998) and a value of 0.34 for bulk copper (Ashby and Jones, 1997). Using alternate residual stress driven structures with bilayer cantilevers, we also measured a residual strain of $(7.1 \pm 0.2) \times 10^{-3}$ on the same copper coatings (Cuddalorepatta et al., 2019). The difference between the residual strain measurements from both techniques is within the uncertainties of the measurements.

4. Scope of proposed design

The proposed method shows that the phenomenon of transverse wrinkling induced in bridges under tensile stretch can be used to measure Poisson's ratio and residual strain in ultra-thin film (thickness < 100 nm). Using the numerical model, the

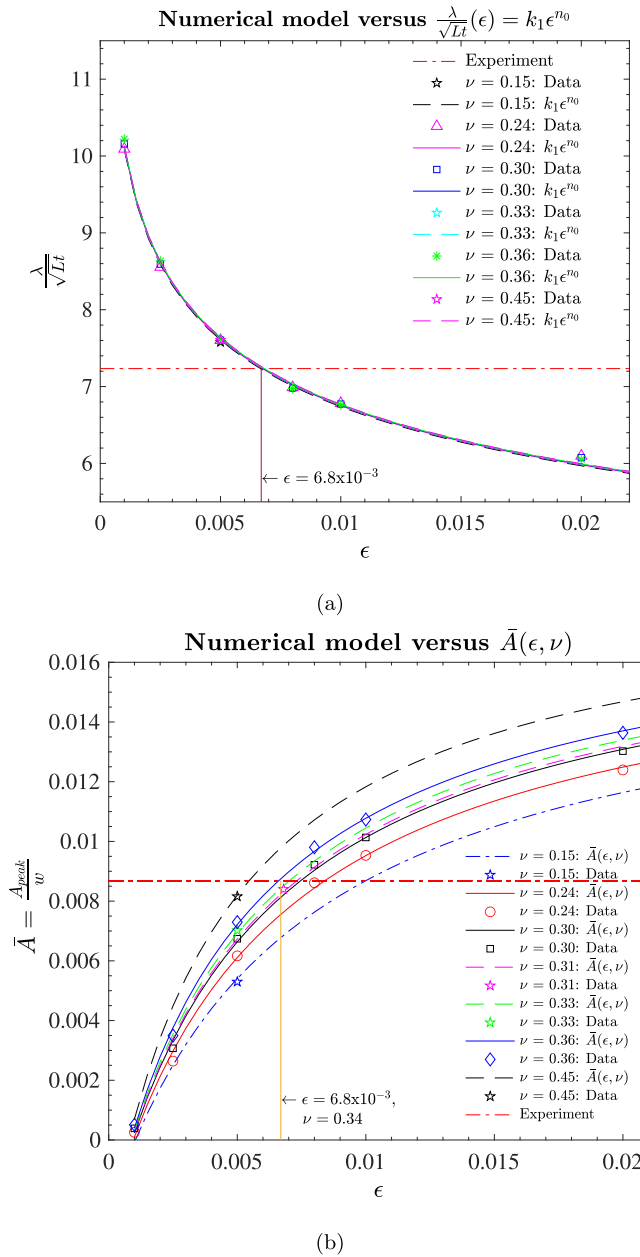


Fig. 8. (a) Normalized wavelength as a function of applied strain and ν . The wavelength is described well with a power law dependence on strain (Eq. 3). The measured wavelength from 65 nm thick copper structures corresponds to a mean residual strain of 6.8×10^{-3} . (b) Normalized peak amplitude as a function of applied strain and ν . The peak amplitude has a non-linear dependence on strain, where the constants have a linear dependence on ν . The measured peak amplitude from 65 nm thick copper structures yields a mean Poisson's ratio of 0.34 for the residual strain of 6.8×10^{-3} measured from (a).

amplitude and wavelength descriptions are determined as a function of the residual tensile strain and Poisson's ratio, for the given geometry. If the boundary conditions and aspect ratios are different from the bridges used in this study, additional simulations are necessary to determine the expressions for the wrinkling parameters. Additional studies that assess the dependence on the geometry and aspect ratios, in addition to the strain and Poisson's ratio will be valuable in providing a generic description of the wrinkling parameters. The properties of ultra-thin films measured using this technique are in agreement with those measured from alternate techniques. As indicated by the uncertainties, the technique is sensitive to small changes in peak amplitude and wavelength. Both parameters can however be accurately measured, thereby providing a simple in-line characterization technique for measuring Poisson's ratio and residual strain of freestanding ultra-thin films in the semi-conductor production line.

Residual stress-driven structures are useful in characterizing material behavior as they are self-driven and do not require complex metrology tools or external loading setup. However, when such structures are fabricated from ultra-thin films, due to the very small thickness the freestanding films tend to collapse or deform during the release from the underlying substrate. By using the proposed geometry of bridges and fabrication protocols, the freestanding structures are robust and yield clean and repeatable deformation with negligible process-induced defects. The proposed fabrication and metrology techniques are simple and can be easily adapted to measure the residual strain and ν of a wide range of thin-film materials with tensile residual stress. With appropriate use of etch stop layers, the proposed design can be extended to films with low selectivity for the XeF₂ etch. The accuracy of the experimental measurement of the wrinkling profiles is dependent in part on the surface roughness of the film. A partial rupture of the freestanding film close to the slits is possible during the Si etch and vent process, making the bridge non-usable. Using the fabrication guidelines provided, however, the thickness and surface condition of the ultra-thin film is preserved during the Si etch process, and, rupture of the freestanding bridges is avoided.

We finally hypothesize the utility of this method in the limit of extremely thin sheets. From the experimental standpoint, a possible limitation would be the feasibility of fabricating freestanding bridges from very thin films without process-induced deformation or rupture. We have fabricated freestanding bridges with thicknesses of 25–50 nm and while this technique could possibly work at these dimensions, it is also dependent on the etch selectivity and spatial uniformity of the residual stress of the material. A future study would be required to investigate this limit, both from a modeling and an experimental perspective. When the thickness becomes extremely small, the sheet would behave more like a membrane and the regularity of the wrinkling patterns might be lost: we might see a transition to folding under the residual strain values imposed here. At this point the inverse problem of finding a Poisson's ratio based on the deformation pattern might not be well-posed anymore.

5. Conclusions

A test methodology for measuring Poisson's ratio and residual strain has been demonstrated for 65 nm copper films. The methodology is applicable to films with a tensile residual stress. The structures are based on the phenomenon in which a thin rectangular strip, when clamped on two sides and stretched in the longitudinal direction develops transverse wrinkling as a result of restricting the Poisson's contraction. Freestanding bridges with in-plane aspect ratios larger than four were successfully fabricated and transverse wrinkling with a decaying amplitude was measured across the width of the bridge. Numerical modeling based on energy minimization methods describe the measured wrinkling behavior of the bridges well. The numerical simulation includes the compliant support condition from the undercut ring in the bridges in the experiment. The numerical results show that the wavelength only depends on strain, not on Poisson's ratio. The amplitude shows a coupled dependence on strain and Poisson's ratio. The proposed technique yields a Poisson's ratio of 0.34 ± 0.05 and a tensile residual strain of $(6.8 \pm 0.8) \times 10^{-3}$ for the wrinkling test structures. The residual strain measured from this technique is in good agreement with that measured from additional residual stress driven test designs developed as part of this study on the same coatings. Poisson's ratio of copper at ultra-thin film thickness (65 nm) is comparable to that at bulk dimensions.

Declaration of competing interest

The authors declare that they have no known competing financial interests or personal relationships that could have appeared to influence the work reported in this paper.

CRedit authorship contribution statement

Gayatri K. Cuddalorepatta: Formal analysis, Methodology, Validation, Visualization. **Wim M. van Rees:** Formal analysis. **Li Han:** Resources. **Daniel Pantuso:** Resources. **L. Mahadevan:** Supervision. **Joost J. Vlassak:** Conceptualization, Methodology, Supervision.

Acknowledgements

The work presented in this paper was supported by [Intel Corporation](#) (SRC contract no. [2014-IN-2476](#)). The test structures were fabricated at the Integrated Sciences Cleanroom and Nanofabrication Facility at Boston College and at the Harvard University Center for Nanoscale Systems (CNS), which is supported by the [National Science Foundation](#) under NSF ECCS award No. [1541959](#), and at the Materials Research Science and Engineering Center at Harvard University, which is supported by the [National Science Foundation](#) under Award No. [DMR-14-20570](#). WMvR thanks the [Swiss National Science Foundation](#) for financial support ([P2EZP2_159091](#), [P300P2_171419](#)) through postdoctoral fellowships.

Appendix A. Fabrication process flow

1. Thin film deposition: Native oxide on the substrate is removed using a buffered oxide etch (5 secs), DI water rinse, N₂ dry. Using a magnetron sputtering system, an argon plasma clean is conducted (20 mT, 25W forward power, 5 min).

Without breaking vacuum, film deposition follows of 2 nm Titanium, 63 nm Copper and 2 nm Titanium (Base pressure of 2×10^{-7} Torr, working pressure of 3 mT, power of 200 W, 99.99% pure targets).

2. Photoresist process: Shipley 1818 photoresist is spin coated using a stepped spin cycle (Cycle 1: speed of 500 rpm for 5 s with a ramp of 100 rpm/s. Cycle 2: speed of 3500 rpm for 30 s with a ramp of 300 rpm/s). The samples are baked on hot plates at 115 °C for 1 min, exposed for 90 s using a maskless aligner followed by a hot plate bake at 115 °C for 1 min. The samples are developed in CD 50 developer for 1 min, rinsed in DI water and dried using N₂.
3. Film etch and photoresist strip: Ti is etched using a reactive ion etching using CF₄ at 100 W, 100 mT, 30 sccm for 1 min. Wet etch of copper follows for 10–15 s in Aluminum Etchant A (80 wt% phosphoric acid, 5 wt% nitric acid, 5 wt% acetic acid and 10% distilled water). The samples are rinsed in DI water at minimal flow rate for less than 20 s and dried using N₂. The photoresist strip uses an acetone and isopropyl alcohol soak for 2 min each in an ultrasound bath. A dehydration bake on a hot plate at 115 °C for about 2 min is conducted followed by a CF₄ REI etch for Ti.
4. XeF₂ isotropic etch in Xactix: A dehydration bake follows on a hot plate at 115 °C for about 2 min. The sample is pumped under vacuum in the loading chamber for 3 h prior to starting the etch process. The pulse time is 20 s for a total number of 150 cycles. XeF₂ gas is not diluted with N₂ during etching. The venting protocol uses a slow N₂ injection rate when the chamber is vented to atmospheric pressure to avoid the collapse and failure of the freestanding bridges. The resulting sample is a stack of 63 nm thick copper film on a 3 nm thick layer of Titanium.

Guidelines for XeF₂ etching: Ultra-thin films are susceptible to rupture if the XeF₂ etching is not conducted in slow pulses, to avoid rapid pressure buildup from reaction gases produced during etching. As the etching process is an exothermic reaction, slow pulses are particularly important to avoid thermal effects on the material behavior. The venting process during the Si etch needs a low nitrogen injection rate to avoid the collapse or bending of the structures. Moisture in the etching chamber and on the sample reacts with the XeF₂ etching gas, leading to the formation of hydrofluoric acid (HF) and a concomitant degradation of the etch selectivity of the test film. A dehydration bake of the samples at 100 °C and pumping down the chamber with the sample for 3 h are necessary prior to initiating the XeF₂ etch. Finally, the structures should be released in a single uninterrupted etch run to avoid exposing the substrate to atmospheric moisture, and, subsequent formation of HF, when the etch process is continued.

Appendix B. Elasticity of thin plates and shells

Geometry We briefly describe the equations for the non-linear elasticity of thin plates and shells as used here. The underlying framework is based on a geometric representation of the mid-surface using parametric coordinates $(x, y) \in U \subset \mathbb{R}^2$ and a map $\bar{m} : U \rightarrow \mathbb{R}^3$ that maps any coordinate pair (x, y) to a location in three-dimensional space $\bar{m}(x, y)$. Based on this map, we can define the normal unit vector at any point on the surface as

$$\bar{n}(x, y) = \left(\frac{\partial \bar{m}}{\partial x} \times \frac{\partial \bar{m}}{\partial y} \right) / \left\| \frac{\partial \bar{m}}{\partial x} \times \frac{\partial \bar{m}}{\partial y} \right\|.$$

The parametric representation of a plate or shell is obtained by extruding the mid-surface along the normal direction, so that we obtain a mapping $\bar{s} : U \times [-h/2, h/2] \rightarrow \mathbb{R}^3$ as

$$\bar{s}(x, y, z) = \bar{m}(x, y) + z\bar{n}(x, y),$$

with $z \in [-h/2, h/2]$.

The map \bar{m} gives rise to a first and second fundamental form of the mid-surface, defined as

$$\mathbf{a}_c = (d\bar{m})^T d\bar{m} = \begin{bmatrix} \bar{m}_x \cdot \bar{m}_x & \bar{m}_y \cdot \bar{m}_y \\ \bar{m}_x \cdot \bar{m}_y & \bar{m}_y \cdot \bar{m}_y \end{bmatrix}$$

and

$$\mathbf{b}_c = -(d\bar{m})^T d\bar{n} = \begin{bmatrix} \bar{m}_{xx} \cdot \bar{n} & \bar{m}_{xy} \cdot \bar{n} \\ \bar{m}_{xy} \cdot \bar{n} & \bar{m}_{yy} \cdot \bar{n} \end{bmatrix}$$

together quantifying the intrinsic properties of the surface, and extrinsic properties of its embedding. We assume that the shell is endowed with an unstrained rest configuration that is characterized by \mathbf{a}_r and \mathbf{b}_r . In this study we consider structures that are initially flat, and so we set $\mathbf{b}_r = 0$ from now on. Using these kinematic quantities, we can define a non-linear elastic energy corresponding to any current embedding \bar{m} and associated first and second fundamental forms \mathbf{a}_c and \mathbf{b}_c

$$E = \frac{1}{2} \int_U \left[\frac{h}{4} \|\mathbf{a}_r^{-1} \mathbf{a}_c - \mathbf{I}\|_e^2 + \frac{h^3}{12} \|\mathbf{a}_r^{-1} \mathbf{b}_c\|_e^2 \right] \sqrt{\det \mathbf{a}_r} \, dx \, dy, \quad (5)$$

where the elastic norm $\|\mathbf{A}\|_e^2 = \alpha \text{Tr}^2(\mathbf{A}) + 2\beta \text{Tr}(\mathbf{A}^2)$ defines the invariants of the strain \mathbf{A} and $\alpha = Y\nu/(1-\nu^2)$ and $\beta = Y/(2+2\nu)$ are the plane-stress Lamé parameters expressed in terms of the Young's modulus Y and Poisson's ratio ν . The underlying material model here is therefore a hyperelastic Saint-Venant Kirchhoff model.

Specializing this formulation for the problem investigated here, we let the parametric coordinates coincide with the Cartesian coordinates in the plane, so that $\mathbf{a}_r = \mathbf{I}$ if the initial configuration has no residual strain. Introducing displacement functions $u(x, y)$, $v(x, y)$ and $w(x, y)$ allows us to write

$$\vec{m}(x, y) = \{x + u(x, y), y + v(x, y), w(x, y)\}^T.$$

From this, we can obtain the stretching contribution to the plate energy density functional

$$\frac{h}{4} \|\mathbf{a}_r^{-1} \mathbf{a}_c - \mathbf{I}\|_e^2 = \frac{Yh}{1-\nu^2} [(\varepsilon_{11} + \varepsilon_{22})^2 - 2(1-\nu)(\varepsilon_{11}\varepsilon_{22} - \varepsilon_{12}^2)],$$

with

$$\begin{aligned} \varepsilon_{11} &= \frac{\partial u}{\partial x} + \frac{1}{2} \left[\left(\frac{\partial u}{\partial x} \right)^2 + \left(\frac{\partial v}{\partial x} \right)^2 + \left(\frac{\partial w}{\partial x} \right)^2 \right] \\ \varepsilon_{12} &= \frac{1}{2} \left(\frac{\partial u}{\partial y} + \frac{\partial v}{\partial x} \right) + \frac{1}{2} \left(\frac{\partial u}{\partial x} \frac{\partial u}{\partial y} + \frac{\partial v}{\partial x} \frac{\partial v}{\partial y} + \frac{\partial w}{\partial x} \frac{\partial w}{\partial y} \right) \\ \varepsilon_{22} &= \frac{\partial v}{\partial y} + \frac{1}{2} \left[\left(\frac{\partial u}{\partial y} \right)^2 + \left(\frac{\partial v}{\partial y} \right)^2 + \left(\frac{\partial w}{\partial y} \right)^2 \right] \end{aligned}$$

Similarly, we get for the bending energy

$$\frac{h^3}{12} \|\mathbf{a}_r^{-1} \mathbf{b}_c\|_e^2 = \frac{Yh^3}{12(1-\nu^2)} [(\kappa_{11} + \kappa_{22})^2 - 2(1-\nu)(\kappa_{11}\kappa_{22} - \kappa_{12}^2)],$$

with

$$\begin{aligned} \kappa_{11} &= \left\{ \frac{\partial^2 u}{\partial x^2}, \frac{\partial^2 v}{\partial x^2}, \frac{\partial^2 w}{\partial x^2} \right\}^T \cdot \vec{n} \\ \kappa_{12} &= \left\{ \frac{\partial^2 u}{\partial x \partial y}, \frac{\partial^2 v}{\partial x \partial y}, \frac{\partial^2 w}{\partial x \partial y} \right\}^T \cdot \vec{n} \\ \kappa_{22} &= \left\{ \frac{\partial^2 u}{\partial y^2}, \frac{\partial^2 v}{\partial y^2}, \frac{\partial^2 w}{\partial y^2} \right\}^T \cdot \vec{n}, \end{aligned}$$

and $\vec{n} = \vec{N}/\|\vec{N}\|$ with

$$\vec{N} = \left\{ -\frac{\partial w}{\partial x} + \frac{\partial v}{\partial x} \frac{\partial w}{\partial y} - \frac{\partial v}{\partial y} \frac{\partial w}{\partial x}, -\frac{\partial w}{\partial y} + \frac{\partial u}{\partial y} \frac{\partial w}{\partial x} - \frac{\partial u}{\partial x} \frac{\partial w}{\partial y}, 1 + \frac{\partial u}{\partial x} + \frac{\partial v}{\partial y} + \frac{\partial u}{\partial x} \frac{\partial v}{\partial y} - \frac{\partial u}{\partial y} \frac{\partial v}{\partial x} \right\}^T$$

These stretching and energy bending functionals are general expressions for the non-linear elastic energy of an initially flat sheet, whose deformed mid-surface is expressed in terms of displacements $u(x, y)$, $v(x, y)$ and $w(x, y)$ from the flat state. It is straightforward to see that the Föppl-von Karman energy can be derived from these expressions by selectively discarding higher order terms (Audoly and Pomeau, 2010, p. 201), in which case the strains and curvatures reduce to

$$\begin{aligned} \varepsilon_{11}^{FvK} &= \frac{\partial u}{\partial x} + \frac{1}{2} \left(\frac{\partial w}{\partial x} \right)^2, & \kappa_{11}^{FvK} &= \frac{\partial^2 w}{\partial x^2}, \\ \varepsilon_{12}^{FvK} &= \frac{1}{2} \left(\frac{\partial u}{\partial y} + \frac{\partial v}{\partial x} \right) + \frac{1}{2} \frac{\partial w}{\partial x} \frac{\partial w}{\partial y}, & \kappa_{12}^{FvK} &= \frac{\partial^2 w}{\partial x \partial y}, \\ \varepsilon_{22}^{FvK} &= \frac{\partial v}{\partial y} + \frac{1}{2} \left(\frac{\partial w}{\partial y} \right)^2, & \kappa_{22}^{FvK} &= \frac{\partial^2 w}{\partial y^2}. \end{aligned}$$

Residual strain If the initial condition contains residual strain, we change the unstrained metric \mathbf{a}_r from its unstrained value $\mathbf{a}_r = \mathbf{I}$ to take into account residual strain. In the work here we consider constant isotropic residual strain fields, and so we define $\mathbf{a}_r^\varepsilon = (1 - \varepsilon^r)^2 \mathbf{I}$. This corresponds to changing the unstrained area of any material element to be $(1 - \varepsilon^r)^2$ times the actual area as measured in its initial realization, so that the material is under constant isotropic stretch. This multiplicative decomposition reduces to the common additive decomposition in the linear theory. To see this, note that in the linear approximation

$$\mathbf{a}_r^\varepsilon = (1 - \varepsilon^r)^2 \mathbf{I} \approx (1 - 2\varepsilon^r) \mathbf{I},$$

and so

$$(\mathbf{a}_r^\varepsilon)^{-1} \approx (1 + 2\varepsilon^r) \mathbf{I}.$$

With this, stretching energy becomes

$$\begin{aligned} \|(\mathbf{a}_r^\varepsilon)^{-1} \mathbf{a}_c - \mathbf{I}\|_e^2 &\approx \|(1 + 2\varepsilon^r) \mathbf{a}_c - \mathbf{I}\|_e^2 \\ &= \|(1 + 2\varepsilon^r)(2\boldsymbol{\varepsilon} + \mathbf{I}) - \mathbf{I}\|_e^2 \\ &\approx \|2(\boldsymbol{\varepsilon} + \varepsilon^r \mathbf{I})\|_e^2, \end{aligned}$$

which shows that after linearization, ε^r is just an additional constant isotropic strain in the energy formulation.

Numerical method Our numerical method implements the energy Eq. (5) using techniques from discrete differential geometry. The mid-surface geometry is defined by a triangle discretization. We follow the shear-free, discrete Kirchhoff description in (Weischedel et al., 2012) to compute the first and second fundamental form for each triangle as a function of its embedding in space, its rest metric \mathbf{a}_r , and its local material properties Y , ν , and h . This enables us to compute the contribution of each individual triangle to the total energy integral (5), and summing over all triangles gives the total energy of the structure. Using a quasi-Newton iterative solver (Liu and Nocedal, 1989) we then minimize the energy as a function of the triangle vertex locations in order to find the mid-surface geometry that minimizes the total energy. As discussed in (Weischedel et al., 2012), the discretization used here can be seen as a geometric reformulation of the constant strain triangle (CST) for the membrane energy, and the Morley element (Morley, 1971) for the bending energy, and therefore closely connects to the finite element community.

Initial condition To create the triangulation of the initial geometry, we use the Triangle library (Shewchuk, 1996). Using this library we can triangulate any planar surface with an arbitrary number of holes, given the externally and internally bounding vertices, according to a specified minimal resolution. For the initial condition considered here, we create a rectangle capped on its two short sides with elliptical arcs, and a symmetric pair of longitudinal slits running along most of the length of the geometry. We run simulations with a total number of triangles varying between 80 000 and 640 000.

Appendix C. Numerical Model Performance: Amplitude versus strain

As described in the main text, it was shown by (Healey et al., 2013), and (Zheng, 2009) that the amplitude of wrinkles in a stretched sheet does not increase monotonically with applied strain, but instead goes through a maximum. We use our solver described above to simulate the wrinkling profile in one of the test cases described in (Healey et al., 2013). In particular, we take a rectangular sheet of dimensions 20×10 , with a thickness of 0.05, and Poisson's ratio $\nu = 0.45$, and stretch it along the x -direction with a varying amount of strain. For each strain we extract the maximum amplitude of the transverse wrinkles and create a bifurcation diagram. The simulations were performed with a grid of 620,000 triangles. Fig. (C.1) shows the bifurcation diagram based on our computations, compared with that of (Healey et al., 2013) using this geometry and Poisson's ratio. Note that the elasticity formulations are not identical, which explains the small difference between the two results. We also remark that in our derivation of Eq. (5) in Appendix B, we assume that in-plane strains are small and so the validity of our results to the $\mathcal{O}(10\%)$ strains shown in the figure needs further verification.

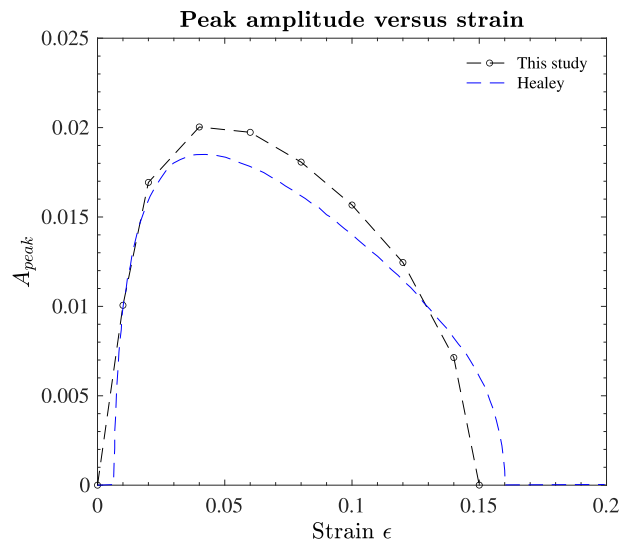


Fig. C.1. Comparison of the peak amplitude versus strain behavior from the current numerical model and (Healey et al., 2013), for $\nu=0.45$ and a maximum strain of 15%. The current study captures the non-monotonic nature of amplitude with strain very well and is in good agreement with Healey's results.

References

- Ager, I., Drory, M., 1993. Quantitative measurement of residual biaxial stress by raman spectroscopy in diamond grown on a ti alloy by chemical vapor deposition. *Phys. Rev. B* 48, 2601–2607.
- Arzt, E., 1998. Size effects in materials due to microstructural and dimensional constraints: a comparative review. *Acta Mater.* 46 (16), 5611–5626.
- Ashby, M.F., Jones, D., 1997. *Engineering Materials I*. Butterworth-Heinemann, Cornwall.
- Audoly, B., Pomeau, Y., 2010. *Elasticity and Geometry. From Hair Curls to the Non-Linear Response of Shells*. Oxford University Press.
- Barai, P., Weng, G.J., 2009. Mechanics of very fine-grained nanocrystalline materials with contributions from grain interior, GB zone, and grain-boundary sliding. *Int. J. Plast.* 25 (12), 2410–2434.
- Cerda, E., Mahadevan, L., 2003. Geometry and physics of wrinkling. *Phys. Rev. Lett.* 90 (7), 074302.
- Chang, J.Y., Yu, G.P., Huang, J.H., 2009. Determination of Young's modulus and Poisson's ratio of thin films by combining $\sin(2\psi)$ x-ray diffraction and laser curvature methods. *Thin Solid Films* 517 (24), 6759–6766.
- Chen, H.-Y., Sastry, A., van Rees, W.M., Vouga, E., 2018. Physical simulation of environmentally induced thin shell deformation. *ACM Trans. Graph.* 37 (4), 1–13.
- Chen, X., Hutchinson, J., 2004. Herringbone buckling patterns of compressed thin films on compliant substrates. *J. Appl. Mech.* 71, 597–603.
- Chung, J., Chastek, T., Fasolka, M., Ro, H., Stafford, M., 2009. Quantifying residual stress in nanoscale thin polymer films via surface wrinkling. *ACS Nano* 3, 844–852.
- Cuddalorepatta, G.K., Sim, G., Li, H., Pantuso, D., Vlassak, J.J., 2019. Residual stress-driven test technique for freestanding ultrathin films: elastic behavior and residual strain. *J. Mater. Res.* 34 (20), 3474–3482. doi:10.1557/jmr.2019.278.
- Efrati, E., Sharon, E., Kupferman, R., 2009. Elastic theory of unconstrained non-euclidean plates. *J. Mech. Phys. Solids* 57 (4), 762–775.
- Freund, L., Floro, J., Chason, E., 1999. Extensions of the Stoney formula for substrate curvature to configurations with thin substrates or large deformations. *Appl. Phys. Lett.* 74, 1987.
- Fu, W.E., Chang, Y.Q., He, B.C., Wu, C.L., 2013. Determination of Young's modulus and Poisson's ratio of thin films by x-ray methods. *Thin Solid Films* 544, 201–205.
- Gunda, M., Kumar, P., Katiyar, M., 2017. Review of mechanical characterization techniques for thin films used in flexible electronics. *Crit. Rev. Solid State Mater. Sci.* 42, 129–152. doi:10.1080/10408436.2016.1186006.
- Hahn, E.N., Meyers, M.A., 2015. Grain-size dependent mechanical behavior of nanocrystalline metals. *Mater. Sci. Eng. A* 646, 101–134.
- Haque, M.A., Saif, M.T.A., 2002. Mechanical behavior of 30–50 nm thick aluminum films under uniaxial tension. *Scr. Mater.* 47 (12), 863–867.
- Healey, T.J., Li, Q., Cheng, R.-B., 2013. Wrinkling behavior of highly stretched rectangular elastic films via parametric global bifurcation. *J. Nonlinear Sci.* 23 (5), 777–805.
- Huang, H., 1998. *Mechanical Properties of Freestanding Polycrystalline Metallic Thin Films and Multilayers*. Harvard University, Cambridge, MA. Ph.D. thesis.
- Huang, H., Spaepen, F., 2000. Tensile testing of free-standing Cu, Ag and Al thin films and Ag/Cu multilayers. *Acta Mater.* 48 (12), 3261–3269.
- Huang, X.F., Liu, Z.W., Xie, H.M., 2013. Recent progress in residual stress measurement techniques. *Acta Mech. Solida Sin.* 26 (6), 570–583.
- Le Rouzic, J., Delobelle, P., Cretin, B., Vairac, P., Amiot, F., 2012. Simultaneous measurement of Young's modulus and Poisson's ratio at microscale with two-modes scanning microdeformation microscopy. *Mater. Lett.* 68, 370–373.
- Liang, L.H., Li, J.C., Jiang, Q., 2002. Size-dependent elastic modulus of Cu and Au thin films. *Solid State Commun.* 121 (8), 453–455.
- Liu, D.C., Nocedal, J., 1989. On the limited memory BFGS method for large scale optimization. *Math Program.* 45 (1–3), 503–528.
- MATLAB Signal Processing Toolbox. Matlab signal processing toolbox. The MathWorks, Natick, MA, USA, (<R2017a>).
- Mei, H., Huang, R., Chung, J., Stafford, C., Yu, H.-H., 2007. Buckling modes of elastic thin films on elastic substrates. *Appl. Phys. Lett.* 90, 151902.
- Morley, L.S.D., 1971. The constant-moment plate-bending element. *J. Strain Anal. Eng. Des.* 6 (1), 20–24.
- Nayyar, V., 2013. *Stretch-Induced Wrinkling in Thin Sheets*. University of Texas at Austin Ph.D. thesis.
- Nayyar, V., Ravi-Chandar, K., Huang, R., 2011. Stretch-induced stress patterns and wrinkles in hyperelastic thin sheets. *Int. J. Solids Struct.* 48 (25), 3471–3483.
- Nayyar, V., Ravi-Chandar, K., Huang, R., 2014. Stretch-induced wrinkling of polyethylene thin sheets: experiments and modeling. *Int. J. Solids Struct.* 51 (9), 1847–1858.
- Oppenheim, A.V., Schaffer, R.W., 2009. *Discrete-Time Signal Processing*. Prentice Hall Press.
- Puntel, E., Deseri, L., Fried, E., 2011. Wrinkling of a stretched thin sheet. *J. Elast.* 105 (1–2), 137–170.
- van Rees, W.M., Matsumoto, E.A., Gladman, A.S., Lewis, J.A., Mahadevan, L., 2018. Mechanics of biomimetic 4D printed structures. *Soft Matter* 14 (43), 8771–8779. doi:10.1039/c8sm00990b.
- van Rees, W.M., Vouga, E., Mahadevan, L., 2017. Growth patterns for shape-shifting elastic bilayers. *Proc. Natl. Acad. Sci.* 114 (44), 11597–11602.
- Sakamoto, H., Park, K., 2005. Design parameters for wrinkle reduction in membrane space structures. In: *Proceedings of 46th AIAA/ASME/ASCE/AHS/ASC Structures, Structural Dynamics and Materials Conference*, p. 1974.
- Senturia, S.D., Howe, R., Mehregany, M., Allen, M., 1987. Microfabricated structures for the in situ measurement of residual stress, Young's modulus, and ultimate strain of thin films. *Appl. Phys. Lett.* 51, 241.
- Shewchuk, J.R., 1996. Triangle: engineering a 2D quality mesh generator and Delaunay triangulator. In: *Applied Computational Geometry Towards Geometric Engineering*. Springer Nature, pp. 203–222.
- Simo, J., Fox, D., 1989. On a stress resultant geometrically exact shell model. Part I: formulation and optimal parametrization. *Comput. Methods Appl. Mech. Eng.* 72 (3), 267–304.
- Stafford, M., Harrison, C., Beers, K., Karim, A., Amis, E., Vanlandingham, M.R., Kim, H.-C., Volksen, W., Miller, R., E.E., S., 2004. A buckling-based metrology for measuring the elastic moduli of polymeric thin films. *Nat. Mater.* 3, 545–550.
- Stoney, G., 1909. The tension of metallic films deposited by electrolysis. *Proc. R. Soc. London Ser. A* 82, 172.
- Talley, C., Clayton, W., Gierow, P., McGee, J., Moore, J., 2002. Advanced membrane materials for improved solar sail capabilities. In: *Proceedings of 43rd AIAA/ASME/ASCE/AHS/ASC Structures, Structural Dynamics and Materials Conference*, p. 1561.
- Vayrette, R., Coulombier, M., Pardoan, T., Raskin, J.P., 2014. On-chip MEMS-based internal stress actuated structures for the mechanical testing of freestanding thin film materials. In: *Advanced Materials Research*, vol. 996. Trans Tech Publications Ltd, Stafa-Zurich, pp. 833–840.
- Vlassak, J.J., Nix, W.D., 1992. A new bulge test technique for the determination of young modulus and poisson ratio of thin-films. *J. Mater. Res.* 7 (12), 3242–3249.
- Weischedel, C., Tuganov, A., Hermansson, T., Linn, J., Wardetzky, M., 2012. Construction of Discrete Shell Models by Geometric finite differences. *Technical Report 220*. Fraunhofer ITWM.
- Wong, W., Pellegrino, S., 2006a. Wrinkled membranes ii: analytical models. *J. Mech. Mater. Struct.* 1 (1), 27–61.
- Wong, W., Pellegrino, S., 2006b. Wrinkled membranes iii: numerical simulations. *J. Mech. Mater. Struct.* 1 (1), 63–95.
- Xiang, Y., Vlassak, J.J., 2006. Bauschinger and size effects in thin-film plasticity. *Acta Mater.* 54 (20), 5449–5460.
- Zheng, L., 2009. *Wrinkling of Dielectric Elastomer Membranes*. California Institute of Technology, Pasadena, CA. Ph.D. thesis.